Dalton Transactions

ROYAL SOCIETY OF CHEMISTRY

PAPER

View Article Online
View Journal | View Issue

Cite this: *Dalton Trans.*, 2024, **53**, 8988

Modulating anti-inflammatory and anticancer properties by designing a family of metal-complexes based on 5-nitropicolinic acid†

Amalia García-García, *[a] Marta Medina-O'donnell,[b] Sara Rojas, [a] Mariola Cano-Morenilla, [b] Juan Morales,[c] María Mar Quesada-Moreno, [c] Juan Sainz,[b,d,e,f] Iñigo J. Vitorica-Yrezabal, [a] Antonio Rodríguez-Diéguez, [a] Amparo Navarro *[c] and Fernando J. Reyes-Zurita*[b]

Received 29th January 2024,
Accepted 3rd April 2024

DOI: 10.1039/d4dt00265b

rsc.li/dalton

A new family of six complexes based on 5-nitropicolinic acid (5-npic) and transition metals has been obtained: $[M(5\text{-npic})_2]_n$ (M^{II} = Mn (**1**) and Cd (**2**)), $[Cu(5\text{-npic})_2]_n$ (**3**), and $[M(5\text{-npic})_2(H_2O)_2]$ (M^{II} = Co (**4**), Ni (**5**), and Zn (**6**)), which display 1D, 2D, and mononuclear structures, respectively, thanks to different coordination modes of 5-npic. After their physicochemical characterization by single-crystal X-ray diffraction (SCXRD), elemental analyses (EA), and spectroscopic techniques, quantum chemical calculations using Time-Dependent Density Functional Theory (TD-DFT) were performed to further study the luminescence properties of compounds **2** and **6**. The potential anticancer activity of all complexes was tested against three tumor cell lines, B16-F10, HT29, and HepG2, which are models widely used for studying melanoma, colon cancer, and liver cancer, respectively. The best results were found for compounds **2** and **4** against B16-F10 (IC_{50} = 26.94 and 45.10 μg mL^{-1}, respectively). In addition, anti-inflammatory studies using RAW 264.7 cells exhibited promising activity for **2**, **3**, and **6** ($IC_{50\ NO}$ = 5.38, 24.10, and 17.63 μg mL^{-1}, respectively). This multidisciplinary study points to complex **2**, based on Cd^{II}, as a promising anticancer and anti-inflammatory material.

Introduction

Over the past few decades, interest in medicinal inorganic chemistry has substantially increased, with emphasis on the development of therapeutic and diagnostic metallodrugs. Metal-containing contrast agents and drugs are administered daily to diagnose and treat a variety of conditions, including infectious diseases, mental disorders, and cancer.[1] One of the most well-known metallodrugs, cisplatin, is widely used to treat many types of cancers. However, due to its dose-dependent toxicity, less toxic analogues, such as carboplatin, oxaliplatin, or lobaplatin, have been developed.[2] Although there has been significant progress in the fight against cancer in recent years, the disease remains as a leading cause of death worldwide. To overcome drug resistance and the side effects of conventional treatments, new medications are required.[3]

Chronic inflammation is closely associated with cancer because inflammatory cells and mediators (*i.e.*, cytokines or prostaglandins) are present in several tumor tissues.[4] While further research is required to fully understand the link between cancer and inflammation, non-steroidal anti-inflammatory drugs (NSAIDs) and selective cyclooxygenase (COX) blockers are common agents administered parallelly to cancer

[a]*Department of Inorganic Chemistry, Faculty of Sciences, University of Granada, Av. Fuentenueva S/N, 18071 Granada, Spain. E-mail: amaliagar@ugr.es*
[b]*Department of Biochemistry and Molecular Biology I, Faculty of Sciences, University of Granada, Av. Fuentenueva S/N, 18071 Granada, Spain. E-mail: ferjes@ugr.es*
[c]*Department of Physical and Analytical Chemistry, Faculty of Experimental Sciences, University of Jaén, Campus Las Lagunillas, 23071 Jaén, Spain. E-mail: anavarro@ujaen.es*
[d]*Genomic Oncology Area, Centre for Genomics and Oncological Research (GENYO), Pfizer-University of Granada-Andalusian Regional Government, Av. de la Ilustración 114, 18016, Granada, Spain*
[e]*Instituto de Investigación Biosanitaria Ibs. Granada, Av. de Madrid 15, 18012, Granada, Spain*
[f]*Consortium for Biomedical Research in Epidemiology and Public Health (CIBERESP), Madrid, Spain*

†Electronic supplementary information (ESI) available: Selected bond lengths and angles of crystal structures, FTIR spectra, photophysical properties, cytotoxicity in cancer cell lines, chemical stability in solution, cytotoxic mechanism (apoptosis), anti-inflammatory studies, elemental analysis, single-crystal X-ray crystallographic data, and theoretical calculations. CCDC 2295415–2295420. For ESI and crystallographic data in CIF or other electronic format see DOI: https://doi.org/10.1039/d4dt00265b

treatment. Nevertheless, the risks of long-term NSAID administration are still unclear.[5] In view of this scenario, combining anticancer and anti-inflammatory properties in a single formulation may help to combat this fatal disease while improving patients' well-being. Furthermore, the design of multifunctional materials with therapeutic and luminescence properties with large Stokes shifts represents an interesting field to be developed for applications such as drugs or fluorescent sensors of pH, polarity, *etc*., in the cellular microenvironment using bioimaging techniques, since it would provide high-contrast images and avoid undesirable reabsorption processes.[6,7]

Combining metal ions with active pharmaceutical agents or biomolecules as ligands is a common approach in medicinal inorganic chemistry to achieve biocompatibility and modulate multiple targets simultaneously.[8] In this work, 5-nitropicolinate (5-npic) was used as a linker because of its similarity to picolinic acid, a metabolic product of L-tryptophan catabolism known for its neuroprotective, immunological, and anti-proliferative effects in the body.[9] In fact, chromium picolinate is widely used as a nutritional supplement for type 2 diabetes patients since chromium is essential for proper carbohydrate and lipid metabolism.[10] Further, Fe^{III}, Ni^{II}, Cu^{II}, Zn^{II}, and Ag^{I} picolinate-based compounds have demonstrated antimicrobial activity.[11,12]

Among all picolinic derivatives, the nitro-substituted metal complexes have received far less attention in the search for novel metal complexes; only four compounds based on 5-npic reported by us[13,69] and some examples focused on 4-nitropicolinic acid and 4-nitropyridine-2-carboxylic-1-oxide acid[14,15] have been published. Additionally, the luminescence of the picolinic skeleton has been studied through lanthanide complexes, showing an intense emission.[16,17] However, no previous in depth studies on the luminescence properties of 5-npic or any other nitro-substituted derivative and their coordination compounds have been described.

Here, novel multifunctional coordination compounds have been synthesized using the 5-npic ligand and a range of transition metals, giving rise to six complexes with the general formulae $[M(5\text{-npic})_2]_n$ (M^{II} = Mn (**1**) and Cd (**2**)), $[Cu(5\text{-npic})_2]_n$ (**3**), and $[M(5\text{-npic})_2(H_2O)_2]$ (M^{II} = Co (**4**), Ni (**5**), and Zn (**6**)). A comprehensive structural and photophysical characterization was performed using single-crystal X-ray diffraction (SCXRD), elemental analysis (EA), and a variety of spectroscopic techniques (Fourier-transform infrared–FTIR, UV-Vis and fluorescence spectroscopy). To shed light on the origin of the luminescence properties of complexes **2** and **6**, quantum chemical calculations using the Time-Dependent Density Functional Theory (TD-DFT) methodology have been carried out. The *in vitro* anticancer activity of all complexes was studied against three tumor cell lines (melanoma B16-F10, colorectal adenocarcinoma HT29, and hepatocellular carcinoma HepG2). The mechanism of action of the two most effective complexes against B16-F10 (complexes **2** and **4**) was subsequently investigated by means of apoptosis, cell cycle arrest, and mitochondrial membrane potential. Finally, the anti-inflammatory activity of each complex was quantified by measuring the final nitrite concentration after incubation of lipopolysaccharide (LPS)-induced RAW 264.7 macrophages.

Results and discussion

Structural description

5-npic ligand displays a variety of coordination modes, as shown in Fig. 1. However, only coordination modes *a* (compounds **1** and **2**), *b* (compound **3**), and *c* (compounds **4–6**) are found in this work.

The complexes could be classified into three groups based on their crystalline structures due to the coordination modes and the different metal centers: compounds **1–2** are 1D structures, compound **3** is a bidimensional framework, and compounds **4–6** are described as mononuclear complexes.

Structure of $[M(5\text{-npic})_2]_n$ (M^{II} = Mn (1) and Cd (2)). The isostructural complexes **1** and **2** consist of monodimensional coordination polymers that crystallize in the monoclinic space group $P2_1$. Two 5-npic molecules and one metal atom set up the asymmetric unit. Each metal center is coordinated to four 5-npic linkers exhibiting a distorted octahedral MN_2O_4 environment. The Mn–O/Cd–O bond distances are in the 2.147(4)–2.176(5) Å/2.252(7)–2.309(7) Å range, whereas the Mn–N/Cd–N bond distances are 2.273(5)–2.295(5) Å/2.323(8)–2.347(8) Å, according to similar published structures.[18–21]

The monodimensional structure is imposed by the coordination mode μ_2-κ^2N1,O2;κO1 (Fig. 1a) of the ligand, which coordinates to a metal ion by the O1 atom of the carboxylate group and also establishes a chelating ring between the O2 atom, the N1 atom from the pyridine ring, and a second metal center. In addition, a 2-fold rotation axis creates two independent ligand molecules, named A and B. While ligand A is perpendicular to the *b* axis and imposes an intermetallic Mn···Mn/Cd···Cd distance of 5.4020(16)/5.3800(11) Å, ligand B is parallel to the *b* axis and creates an intermetallic distance of 5.2960(5)/5.4093(6) Å. The chain is made up of ligands A and B arranged in triangles (Fig. 2) and propagates along the *b* axis, giving rise to 1D polymers. Table S1† provides details of selected bond lengths and angles of all complexes.

Structure of $[Cu(5\text{-npic})_2]_n$ (3). Complex **3** is a bidimensional polymer that belongs to the monoclinic $P2_1/c$ space group. The asymmetric unit contains half of a Cu^{II} atom and one ligand

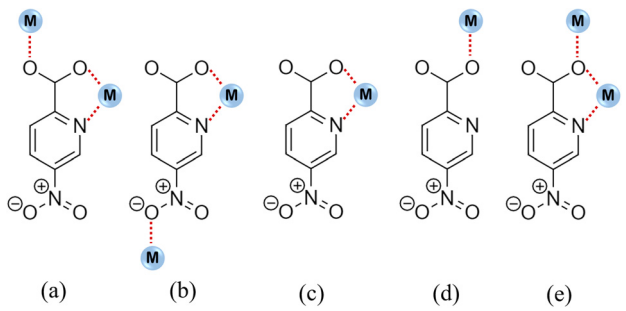

Fig. 1 Coordination modes of 5-nitropicolinate.

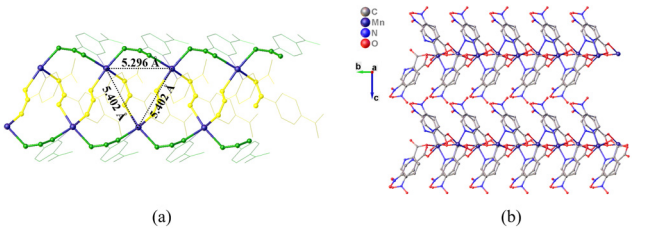

Fig. 2 (a) Details of the intermetallic Mn···Mn distances imposed by ligands A (yellow) and B (green) along the chain. (b) Chains run parallel to the *b* crystallographic axis. Hydrogen atoms have been omitted for clarity.

molecule. Each Cu^{II} atom is coordinated to four 5-npic ligands in the octahedral geometry of CuN_2O_4 because of the inversion center in the metallic ion. Furthermore, the coordination sphere undergoes a large deformation, which results from the high Jahn–Teller effect around the d-orbitals of Cu^{II}. Consequently, the apical bond is elongated to 2.708(4) Å (van der Waals nature),[22,23] whereas the basal bonds are similar to already published structures.[24,25] The ligand displays the coordination mode μ_2-κ^2N1,O1;κO4 (Fig. 1b), chelating a Cu^{II} atom through N1 and O1 atoms of the picolinic moiety and coordinating a second metal atom by the nitro group. This gives rise to sheets parallel to the [−102] plane (Fig. 3). To the best of our knowledge, this is the first complex based on a nitropicolinic derivative in which a nitro group is involved.

Structure of $[M(5\text{-npic})_2(H_2O)_2]$ (M^{II} = Co (4), Ni (5), and Zn (6)). All these compounds are structurally identical and they crystallize in the monoclinic group $P2_1/n$. The structures are made of neutral monomers linked together by hydrogen bonds. The asymmetric unit is formed of half of the metal center, one ligand molecule, and one coordinated water molecule. Due to the inversion center located in the metal ion, this atom is overall coordinated to two water molecules and two 5-npic ligands through the bidentate coordination mode μ-κ^2N1,O1 (Fig. 1c). This results in an octahedral environment in MN_2O_4. The M–O and M–N bond lengths are comparable to those of other picolinic-derivative compounds.[26–29]

The mononuclear units are linked together *via* O–H···O hydrogen bonds thanks to the coordinated water molecules, whose bond distances are shown in Table S2.† Finally, the

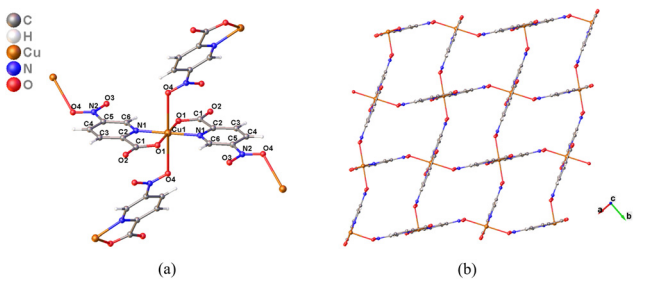

Fig. 3 (a) Details of the coordination sphere in **3**. (b) Perspective view of the sheet along the *c* axis.

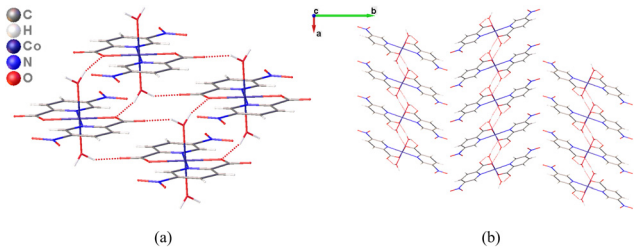

Fig. 4 (a) The coordinated water molecules in complexes **4–6** allow the mononuclear entities to interact with one another through O–H···O hydrogen bonds. (b) Glide planes perpendicular to the *b* axis create a zigzag disposition of the monomers. Hydrogen bonds are represented in dotted red lines.

glide planes lead to a zigzag pattern of the monomers in the supramolecular structure (Fig. 4).

Infrared (IR) spectroscopy

Fig. S1† displays the IR spectra of each compound and 5-npic, and the main bands are compared in Table S3.† In the ligand spectrum, the characteristic aromatic C–H bond bands are visible at 3090–3078 cm^{-1}, remaining almost constant in the complexes' spectra. Since it is challenging to correlate the tension bands of the C=O, N–O, and C=C bonds, an approximation has been made. The first band at 1728–1699 cm^{-1} due to the stretching vibrations of the C=O bond of the carboxylic acid shifts to 1670–1629 cm^{-1} in the complexes' spectra. Additionally, the peak at 1288 cm^{-1} from the C–N bond of the pyridine ring shifts to 1346–1267 cm^{-1} in the spectra of the complexes. This suggests that the nitrogen atom of the pyridine ring and the carboxylic group of the ligand are both responsible for the coordination with the metal atom.[30]

The peaks attributed to the N–O bond vibration remain constant with the exception of complex **3**, which exhibits a band displacement due to the asymmetric and symmetric vibration of the N–O bond with respect to the ligand's spectrum. This fact supports the coordination of Cu^{II} through the nitro group.

The broad band that appears around 3200 cm^{-1} in the spectra of complexes **4–6** indicates the presence of water molecules in those structures.

Photophysical properties

Complexes based on d^{10} metal ions are of great interest for their luminescence properties and potential applications in cell bioimaging. A few luminescent Cd^{II} and Zn^{II} complexes have been published with bioimaging application and interesting *in vitro* antiproliferative activities against cancerous cell lines.[31–33] Thus, photophysical studies were carried out for complexes **2** and **6**, containing Cd^{II} and Zn^{II}, respectively.

Absorption spectra of **2**, **6**, and 5-npic ligand were explored in solution (Fig. S2†). All three showed similar spectral profiles, with a strong band at 209 nm and two weaker bands around 283 and 248 nm. The large Stokes shift around 17 046 cm^{-1} opens the possibility of exploring the application

of these novel compounds as fluorescent drugs and for their cellular localization using bioimaging techniques. Following that, fluorescence emission spectra in solid samples (Fig. 5) displayed a sharp profile with a prominent peak at 485 nm (2.56 eV). The similarity between the three spectral profiles indicates that the luminescence properties of the ligand remain almost intact after complexation. The slight decrease in the emission intensity could be due to additional energy loss pathways such as magnetic perturbations, redox activity or electronic energy transfer.[34]

To determine which electronic transitions are responsible for the photophysical properties, the molecular geometries in the ground state were optimized and the vertical electronic transitions were computed for **2**, **6**, and 5-npic as described in the Theoretical Calculation section using DFT and TD-DFT methodologies, respectively. First, the molecular geometry of 5-npic was optimized considering three conformations depending on the orientation of the carboxylic group (Fig. S3†). Table S4† lists the relative energies for the three conformers, showing that **conformer 3** is the most stable both in the gas phase and in solution.

In order to facilitate the assignment of the electronic transitions, Fig. S4† shows the experimental absorption spectrum of 5-npic in water solution along with the vertical electronic transitions calculated at the TD-CAM-B3LYP/6-31G** level of theory. The band in the absorption spectrum at 283 nm could be assigned to the $S_0 \rightarrow S_4$ electronic transitions calculated at 249 nm (f = 0.25) being HOMO−1 → LUMO with 88% contribution (Fig. S5†). The other two bands at 248 and 209 nm could be assigned to $S_0 \rightarrow S_6$ (calculated at 226 nm) and $S_0 \rightarrow S_{10}$ (186 nm) transitions, respectively. Some selected electronic transitions with significant oscillator strengths are listed in Table S5.†

The fluorescence emission of the ligand was calculated in the gas phase and in water solution. Although the excited states S_4, S_6, and S_{10} were predicted to be the most populated during the absorption process, the molecule relaxes to the excited state S_1 and a Kasha-type emission occurs from it. As shown in Table S6,† the calculated emission is predicted at 610 nm in the gas phase and at 523 nm in water solution, the latter being closer to the experimental observation.

For complex **6**, the molecular geometry of an isolated monomer was optimized in water solution. Fig. 6 shows the experimental absorption spectrum in water solution along with the theoretical vertical electronic transitions. According to the TD-DFT calculations (Table S7†), the lowest energy transition appearing at 283 nm could be assigned to the $S_0 \rightarrow S_7$ electronic transitions calculated at 271 nm with the contributions of HOMO−8 → LUMO (43%) and HOMO−4 → LUMO (41%). The other two bands at 249 and 214 nm in the absorption spectrum could be assigned to the transitions predicted at 251 nm ($S_0 \rightarrow S_{11}$) and 165 nm ($S_0 \rightarrow S_{66}$).

On the other hand, the vertical electronic transitions were also computed using the ONIOM method (Table S8†). In this method, the experimental bands in the absorption spectrum could be assigned to the transitions calculated at 271 nm ($S_0 \rightarrow S_9$), 242 nm ($S_0 \rightarrow S_{15}$), and 186 nm ($S_0 \rightarrow S_{43}$). Thus, the ONIOM method only improves the results for the most intense band observed at 214 nm with respect to the individual complex calculations.

Regarding the fluorescence emission, even though it is predicted that the most populated states during the absorption process would be S_{15}, S_{24}, and S_{43}, the molecule relaxes to lower excited states and the emission occurs from the S_1/S_2 states. Table 1 shows that the band at 485 nm is predicted at 439 nm (ΔE = 0.27 eV) using the ONIOM method and at 566 nm in the gas phase and water solution (ΔE = 0.37 eV) if the monomer is modelled.

The molecular orbitals involved in the electronic transition $S_2 \rightarrow S_0$ are shown in Fig. 7. As can be seen, the LUMO+1 orbital is delocalized on a ligand molecule, whereas the

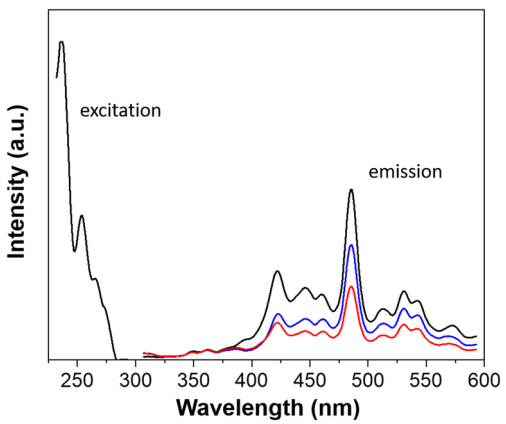

Fig. 5 Excitation and fluorescence emission spectra in solid samples of the 5-npic ligand (black), compound **2** (blue), and **6** (red).

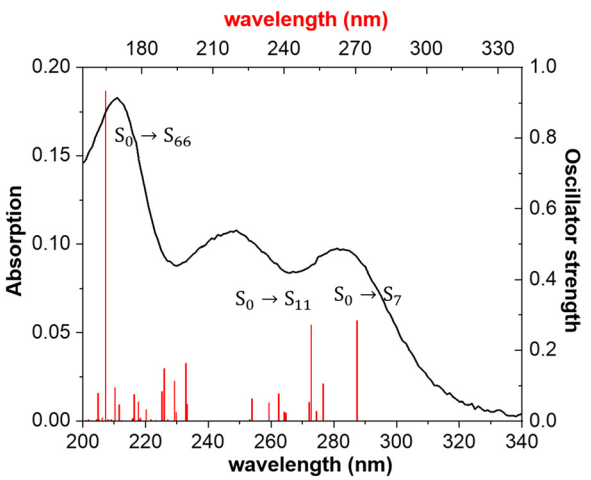

Fig. 6 Experimental absorption spectrum along with the oscillator strength of the vertical electronic transitions calculated at the TD-CAM-B3LYP-D3/6-31G**+LANL2DZ level of theory in water solution for the monomer of **6**. The bottom axis refers to the experimental absorption spectrum and the top axis to the calculated electronic transitions.

Table 1 Experimental emission (λ^{exp}_{emis}), theoretical transition ($\lambda^{calc}_{vert-emis}$), and oscillator strength (f) for the $S_n \rightarrow S_0$ (≥15%) calculated at the ONIOM (CAM-B3LYP-D3:PM6) level of theory for **6** (LANL2DZ for Zn, 6-31G** for C, H, N, and O)

Phase	eV (nm) (λ^{exp}_{emis})	eV (nm) ($\lambda^{calc}_{vert-emis}$)	Transition	*f*	% Contribution
Monomer CAM-B3LYP-D3					
Gas	2.56 (485)	2.19 (566)	$S_1 \rightarrow S_0$	0.00	LUMO → HOMO (82%)
Water	2.56 (485)	2.19 (566)	$S_1 \rightarrow S_0$	0.00	LUMO → HOMO−2 (88%)
ONIOM(CAM-B3LYP-D3:PM6)					
Gas	2.56 (485)	2.83 (439)	$S_2 \rightarrow S_0$	0.00	LUMO → HOMO−1 (40%) LUMO+1 → HOMO (40%)

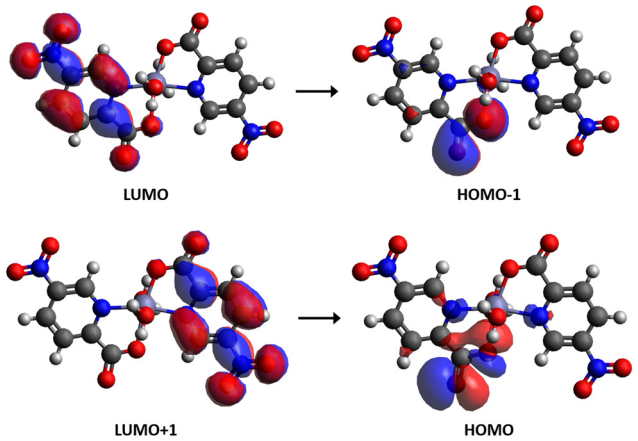

Fig. 7 Representation of the molecular orbitals (isocontour plots 0.02 a.u.) involved in the electronic transition $S_2 \rightarrow S_0$ calculated at the ONIOM(CAM-B3LYP-D3:PM6) level of theory for complex **6**.

HOMO is located on the carboxylate group of the other ligand (with 40% contribution). On the other hand, the LUMO delocalizes on a ligand molecule, while HOMO−1 resides on the carboxylate group of the same ligand (40% contribution). The electron density of these molecular orbitals exhibits no contribution of the Zn^{II} atom, which is consistent with the similarity between the experimental emission spectrum of the free ligand and the complex **6**.

For complex **2**, Fig. 8 shows the experimental absorption spectra along with the theoretical vertical electronic transitions for the fragments, whereas Table S9† lists the vertical electronic transitions calculated for both models, **f1Cd** and **f4Cd**. Both models yield very similar results. For **f1Cd**, the most intense transitions calculated around 266 ($S_0 \rightarrow S_{45}$), 256 ($S_0 \rightarrow S_{57}$) and 254 ($S_0 \rightarrow S_{60}$), and 236 nm ($S_0 \rightarrow S_{76}$) correspond to the experimental bands observed at 283, 249, and 214 nm, respectively. In the case of model **f4Cd**, the main transitions are predicted at 256 ($S_0 \rightarrow S_{132}$), 252 ($S_0 \rightarrow S_{147}$), and 233 nm ($S_0 \rightarrow S_{238}$).

Finally, the calculated emission for **f1Cd** and **f4Cd** fragments are summarized in Table 2. As for the free ligand and compound **6**, a Kasha-type emission occurs from the first excited state S_1. As can be observed, both models acceptably predict the experimental maximum at 485 nm. However, when calculating the transition $S_1 \rightarrow S_0$, model **f1Cd** is slightly closer to the experimental result, with 71% contribution from LUMO to HOMO−2. The LUMO is delocalized in a 5-npic molecule, while HOMO−2 is centered on its carboxyl group (Fig. 9), without the participation of the Cd^{II} atom. This is consistent

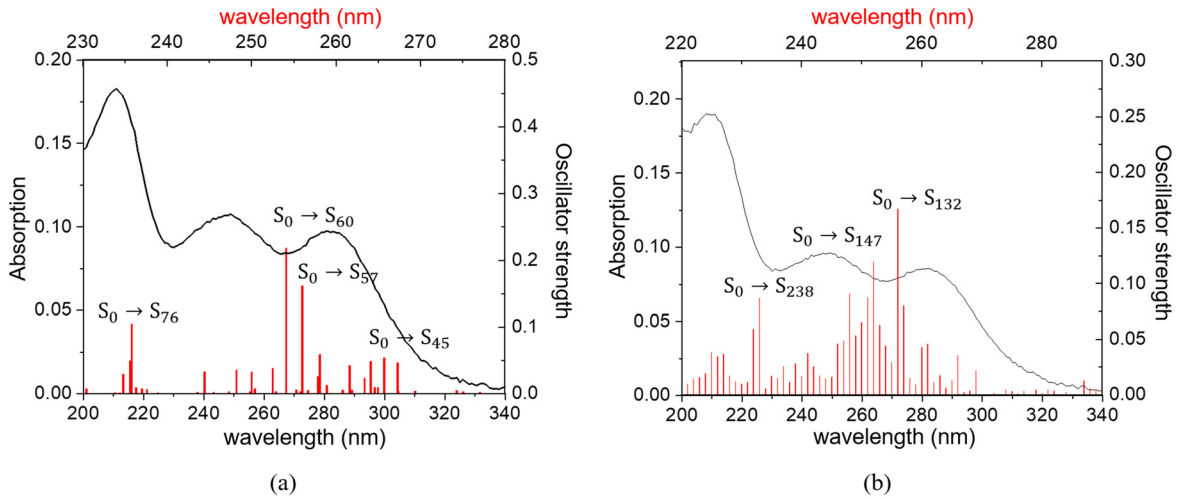

Fig. 8 Experimental absorption spectra along with the oscillator strength of the vertical electronic transitions calculated at the TD-CAM-B3LYP-D3/6-31G**+LANL2DZ level of theory for (a) the model **f1Cd** and (b) **f4Cd** of complex **2**. The bottom axis refers to the experimental absorption spectrum and the top axis to the calculated electronic transitions.

Table 2 Experimental emission (λ^{exp}_{emis}), theoretical transition ($\lambda^{calc}_{vert-emis}$), and oscillator strength (f) for the $S_1 \rightarrow S_0$ (≥15%) calculated at the ONIOM (CAM-B3LYP-D3:PM6) level of theory for complex **2** (LANL2DZ for Cd, 6-31G** for C, H, N, and O)

Fragment	eV (nm) (λ^{exp}_{emis})	eV (nm) ($\lambda^{calc}_{vert-emis}$)	Transition	f	% Contribution
f1Cd	2.56 (485)	2.49 (499)	$S_1 \rightarrow S_0$	0.01	LUMO → HOMO−2 (71%)
f4Cd	2.56 (485)	2.89 (429)	$S_1 \rightarrow S_0$	0.01	LUMO+1 → HOMO−2 (44%)

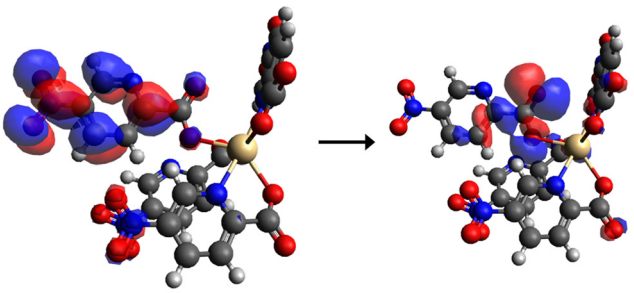

Fig. 9 Representation of the molecular orbitals (isocontour plots 0.02 a.u.) involved in the electronic transition $S_1 \rightarrow S_0$ for the fragment **f1Cd** of complex **2**.

with the similarity between the experimental emission spectrum of the free ligand and that of complex **2**.

Cytotoxicity in cancer cell lines

Significant antitumoral effects have been reported by several metal complexes (Cu^{II}, Ru^{II}, Re^{I}, Os^{II}, Ir^{III}, Pt^{IV}, and lanthanides) based on picolinic acid derivatives.[35–45] Furthermore, we have previously shown that the nitro group could improve the anticancer properties of an organic ligand.[46] For all of these reasons, the cytotoxic activity of complexes **1–6** and free 5-npic ligand against three cancer cell lines (B16-F10-murine melanoma cells, HT29-colon-cancer cells, and HepG2-hepatoma cells) was determined using 3-(4,5-dimethylthiazol-2-yl)-2,5-diphenyltetrazolium bromide (MTT) assay. Table 3 shows how most of the compounds are able to inhibit cell growth after 72 h with values between 5.55–78.47 μg mL^{-1} for IC_{20}, 26.94–86.55 μg mL^{-1} for IC_{50}, and 76.17–100.94 μg mL^{-1} for IC_{80}. In particular, 66% of the products were more cytotoxic than the free ligand at IC_{50} in B16-F10 and HT29 cells; however, the complexes did not enhance the cytotoxicity of the ligand in HepG2 cells. Compared to commercial drugs like cisplatin, which presents IC_{50} values ranging from 23 μM (in B16-F10 cells)[47] to 45.6 μM (in HepG2 cells),[48] the compounds here reported have slightly lower cytotoxic potential. However, this fact should not necessarily be a hindrance since high-cytotoxic drugs could produce a large number of side effects that restrict their dosage and, hence, their efficacy. In clinical practice, the toxicity profile of cisplatin includes nausea and vomiting, renal dysfunction, neurotoxicity, and ototoxicity.[49]

Among all the complexes, compounds **2** and **4** exhibited the highest antitumoral activity, particularly against the B16-F10 cell line, with IC_{50} values of 26.94 ± 4.91 and 45.10 ± 3.84 μg mL^{-1} for **2** and **4**, respectively (Fig. S6†).

Table 3 Cytotoxicity of complexes **1–6** and their ligands against B16-F10, HT29, and HepG2[a]

Cell line	Compound	IC_{20} (μg mL^{-1})	IC_{50} (μg mL^{-1})	IC_{80} (μg mL^{-1})
B16-F10	5-npic	49.61 ± 2.04	66.89 ± 3.07	88.29 ± 3.15
	1	118.83 ± 32.50	N/A[b]	N/A[b]
	2	5.55 ± 2.81	26.94 ± 3.53	76.17 ± 3.83
	3	37.01 ± 2.03	48.91 ± 3.53	N/A[b]
	4	19.56 ± 2.99	45.10 ± 3.84	80.48 ± 2.43
	5	39.22 ± 9.39	74.64 ± 4.38	101.09 ± 0.76
	6	41.48 ± 6.08	64.22 ± 4.07	91.47 ± 12.01
HT29	5-npic	37.12 ± 3.80	60.56 ± 3.68	110.53 ± 3.67
	1	42.85 ± 5.63	42.29 ± 1.93	N/A[b]
	2	37.60 ± 4.55	61.96 ± 3.46	95.46 ± 2.37
	3	39.62 ± 3.10	64.60 ± 3.26	103.37 ± 0.60
	4	39.95 ± 2.94	53.33 ± 2.24	N/A[b]
	5	34.27 ± 3.74	51.39 ± 1.07	91.25 ± 6.62
	6	40.23 ± 1.02	48.55 ± 0.80	N/A[b]
HepG2	5-npic	12.14 ± 5.89	48.87 ± 11.33	106.74 ± 8.94
	1	78.47 ± 1.58	83.37 ± 2.25	105.60 ± 10.00
	2	26.25 ± 6.41	66.32 ± 4.48	103.01 ± 5.27
	3	72.39 ± 3.92	86.55 ± 4.49	100.94 ± 0.87
	4	41.76 ± 13.33	76.77 ± 7.03	102.29 ± 0.94
	5	17.62 ± 9.42	62.72 ± 5.17	112.77 ± 5.35
	6	33.54 ± 8.24	72.96 ± 2.84	106.70 ± 2.05

[a] Cells were treated with the complexes for 72 h at doses ranging from 0 to 100 μg mL^{-1}. Each point represents the mean value ± SD of at least two independent experiments performed in triplicate. [b] N/A = not available.

To shed light on the mechanism of action of the complexes, their chemical stabilities were investigated by measuring their crystallinity retention after 72 h in phosphate-buffered saline (PBS) solution using powder X-ray diffraction (PXRD). As shown in Fig. S7,† all compounds, except **4**, nearly maintained their crystallinity, although the characteristic peaks of NaCl from PBS at 31.6 and 45.3° were slightly evident. On the other hand, given that the most toxic heavy metals for humans are mercury, lead, chromium, cadmium, and arsenic,[50] it seems reasonable to think that compound **2** should exhibit a high antitumoral effect. Furthermore, Cd^{II} has the largest ionic radius and thus, the longest coordination bonds. This, combined with the fact that Cd^{II} is a soft Lewis acid, makes its complexes less stable.[51] In the case of Co^{II}, it is an essential metal for the organism, but at higher concentrations it causes toxicity.[52] Moreover, complex **4** exhibited low stability after 72 h as it degrades completely. This feature may increase the toxicity and thus, the antitumoral activity of this compound.

Due to the results, compounds **2** and **4** were selected to investigate their apoptotic potential effect, cell cycle distribution, and mitochondrial membrane potential effect in the B16-F10 cell line.

Cytotoxic mechanism. In order to determine whether the cytotoxicity caused by the coordination compounds activates the apoptotic process in the B16-F10 cell line, the percentage of apoptotic cells by double staining with annexin-V FITC and propidium iodine (PI) using a fluorescence-activated cell sorter (FACS) flow cytometer was measured. Complexes **2** and **4** exhibited a higher percentage of the apoptotic effect compared to necrosis on treated cells. At IC_{50}, compound **2** exhibited 36.67% of total apoptosis (early apoptotic together with late apoptotic cells), whereas **4** showed 27.33% (Fig. 10 and Fig. S8†). As the number of apoptotic cells increased in a dose-dependent manner, at IC_{80} these percentages were higher: total apoptosis of 93.95% for **2** and 58.40% for compound **4**.

Furthermore, after 72 h of incubation with **2** and **4** at IC_{80}, phase-contrast light microscopy cell images (Fig. 11) demonstrated the characteristics apoptotic morphological changes triggered in B16-F10 cells, such as cell shrinkage, loss of normal cell architecture, disruption of cell-membrane integrity, *etc*. It is noteworthy that compound **2** exhibits a high total apoptosis value at IC_{80} (93.95%), suggesting the potential of this complex as a promising anticancer drug.

Cell cycle arrest. Cell-cycle distribution and cell cycle arrest were investigated after 72 h of treatment with compounds **2** and **4** at IC_{50} and IC_{80} against B16-F10 murine melanoma cells. The DNA histogram analysis (Fig. 12) revealed that compared to the control, compound **4** significantly increased the proportion of cells in the G0/G1 phase 1.5 times at IC_{50} and 1.4 times at IC_{80} (83.28 ± 1.91% and 77.99 ± 1.31% at IC_{50} and IC_{80}, respectively).

Conversely, the percentages of cells in phase S decreased by 3.8 and 1.8 times at IC_{50} and IC_{80}, respectively (9.60 ± 2.31% at IC_{50} and 20.22 ± 1.33% at IC_{80}). The changes in the G2/M phase for this product were less significant. On the other hand, treatment with complex **2** did not present significant changes in any phases of the cell cycle compared to the control, except a slight decrease in the G2/M phase. According to these results, the treatment with compound **4** in B16-F10 cancer cells resulted in cell cycle arrest in the G0/G1 phase, which could indicate a cytostatic or differentiation process.

Changes in the mitochondrial membrane potential (MMP). In order to propose possible apoptotic pathways triggered by complexes **2** and **4** against B16-F10 cancer cells, changes and disruptions in the MMP were studied by flow cytometry using double staining with Rh123 and PI (see Experimental section for further details). The two main processes that are activated during apoptosis are the intrinsic apoptotic pathway, which causes mitochondrial alteration and MMP loss, and the extrin-

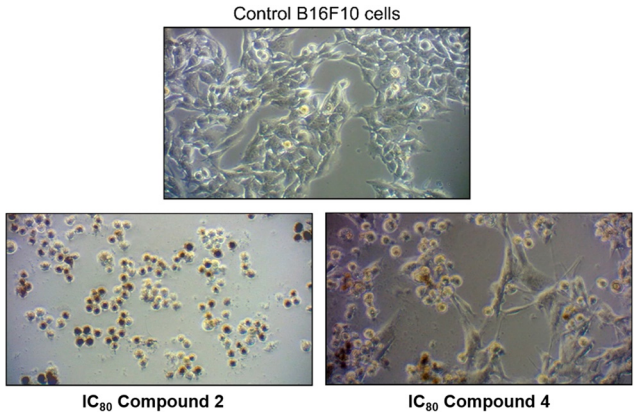

Fig. 11 Microscopic optical photographs. Morphological changes in B16-F10 cells after exposure for 72 h to **2** and **4** at their IC_{80} values.

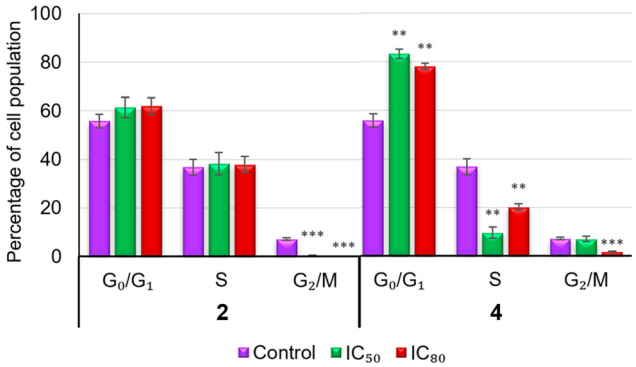

Fig. 12 Percentage of B16-F10 cells in each phase of the cell cycle after treatment with compounds **2** and **4** at IC_{50} and IC_{80} for 72 h. Values are expressed as the mean ± SD of two independent experiments performed in triplicate.

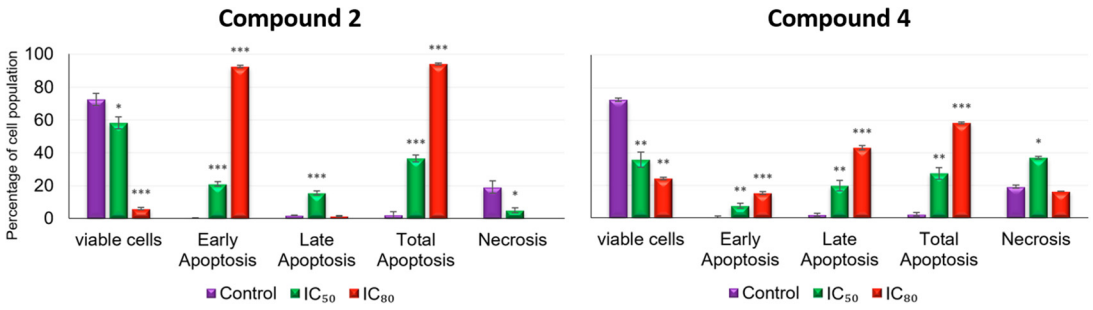

Fig. 10 *In vitro* mechanistic studies of the cytotoxicity of compounds **2** and **4** using flow cytometry analysis of Annexin V-FITC staining and PI accumulation at IC_{50} and IC_{80}: viable cells (Annexin V− and PI−), early apoptotic cells (Annexin V+ and PI−), late apoptotic cells (Annexin V+ and PI+), and necrotic cells (Annexin V− and PI+). Values represent the mean ± S.E.M. of duplicate independent experiments, performed in triplicate.

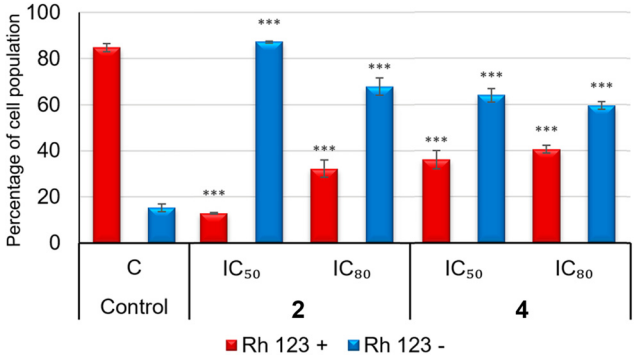

Fig. 13 Flow-cytometry analysis of Rh123 and PI staining after exposure of B16-F10 cells to complexes **2** and **4** at their IC_{50} and IC_{80} for 72 h. Rh123 positive cells (red bars) were Rh123+ with PI+ or PI−. Rh123 negative cells (blue bars) were Rh123− with PI− or PI+. Values are expressed as the mean ± SD of two independent experiments performed in triplicate.

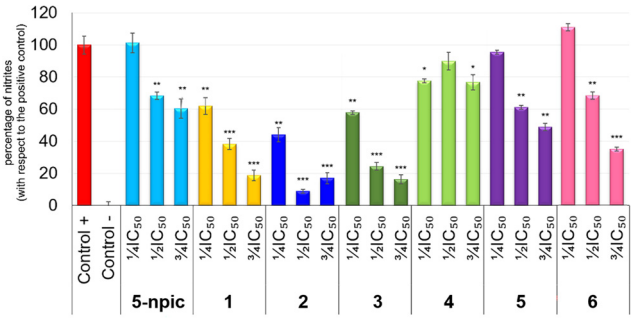

Fig. 14 Effect of free 5-npic and complexes **1–6** on the release of nitrites in RAW 264.7 murine macrophage cells. Positive control means only LPS treated control cells, while negative control are untreated cells. The compounds were incubated for 48 h at $\frac{3}{4}$ IC_{50}, $\frac{1}{2}$ IC_{50}, and $\frac{1}{4}$ IC_{50}. The data represent the mean ± SD of at least two independent experiments performed in triplicate. Key: (**) $p < 0.01$ and (***) $p < 0.001$, with respect to the positive control.

sic pathway, which induces apoptosis without changes in the MMP. The results showed a notable increase in the number of negative Rh123 cells after B16-F10 cells were treated with **2** and **4** for 72 h at IC_{50} and IC_{80}, indicating an intrinsic apoptotic pathway activation for both complexes (Fig. 13).

Anti-inflammatory studies

Firstly, sub-cytotoxic concentrations were established to ensure that the anti-inflammatory effects were caused by an inflammatory process rather than the cytotoxicity of compounds **1–6** against macrophage/monocyte murine RAW 264.7 cells (Table S10†). Based on these results, the $\frac{3}{4}$ IC_{50}, $\frac{1}{2}$ IC_{50}, and $\frac{1}{4}$ IC_{50} values were used for the determination of the anti-inflammatory response.

In the inflammatory process, RAW 264.7 macrophages play an important role producing inflammation mediators such as nitric oxide (NO), which is generated by the enzyme nitric-oxide synthase (iNOS). Lipopolysaccharide (LPS)-induced RAW 264.7 can activate iNOS, and the resulting NO could be easily oxidized to nitrite. Therefore, the anti-inflammatory activity of complexes **1–6** in LPS-induced RAW 264.7 was investigated by measuring the nitrite concentration (see Experimental section for further details). According to the results shown in Fig. 14, most of the coordination compounds considerably reduced the NO production, with a percentage of NO inhibition between 65 and 83% at $\frac{1}{2}$ IC_{50} and $\frac{3}{4}$ IC_{50}. When tested at $\frac{1}{2}$ IC_{50}, **2** showed the highest NO inhibition (91%), followed by **3** (75.5%), **1** (61.6%), and **6** (31.42%). Additionally, complex **2** exhibited the highest inhibition (56%) at the lowest concentration of $\frac{1}{4}$ IC_{50} (5.42 μg mL^{-1}), demonstrating its potential in inflammatory processes.

In order to complete the study of the anti-inflammatory potential of the compounds, the concentration that reduces NO production to 50% ($IC_{50\ NO}$) was calculated after 48 h of treatment (Table 4). The results indicate that compounds **2**, **3**, and **6** had $IC_{50\ NO}$ values lower than that of the ligand (5.38 ± 0.04, 24.10 ± 1.74, and 17.63 ± 0.07 μg mL^{-1} for compounds **2**, **3**, and **6**, respectively). Among them, compound **2** showed the lowest $IC_{50\ NO}$ value, which made it 5.4-fold more effective than the free ligand.

Table 4 $IC_{50\ NO}$ values of **1–6** and 5-npic after 48 h of treatment in RAW 264.7 cells

Compound	$IC_{50\ NO}$ (μg mL^{-1})	IC_{50} of ligand/IC_{50} of compound
5-npic	30.36 ± 2.41	1
1	40.98 ± 5.85	0.74
2	5.38 ± 0.04	5.64
3	24.10 ± 1.74	1.26
4	65.76 ± 4.60	0.46
5	32.52 ± 2.12	0.93
6	17.63 ± 0.07	1.72

Experimental

Synthesis of metal complexes

All reagents were purchased from Sigma-Aldrich and used as received without additional purification.

Compounds **1–6** were obtained by a solvothermal route through the following procedure: 0.03 mmol of corresponding metal salt ($MnCl_2{\cdot}4H_2O$ (**1**), $CdSO_4$ (**2**), $CuSO_4{\cdot}5H_2O$ (**3**), $Co(NO_3)_2{\cdot}6H_2O$ (**4**), $NiCl_2{\cdot}6H_2O$ (**5**), and $Zn(NO_3)_2{\cdot}6H_2O$ (**6**)) were dissolved in a mixture of 0.5 mL of *N*,*N*-dimethylformamide (DMF) and 0.5 mL of distilled water, with the exception of **2** for which only 1 mL of H_2O instead was used. Separately, 0.06 mmol of 5-npic ligand were dissolved in a hot mixture of 0.5 mL of DMF and 0.5 mL of H_2O to prevent its precipitation. Then, the metal salts were added to the ligand solution in glass vessels, which were then closed and introduced in an oven at 95 °C. One hour later, crystalline powders precipitated, and after a total reaction time of 24 h crystals of different colors (yellow (**1**), white (**2**), dark blue (**3**), orange (**4**), light green (**5**), and white (**6**)) were obtained by filtration, washed with distilled water and dried under an air atmosphere.

Elemental analyses of all obtained materials were performed (Table S11†).

Physicochemical characterization

Elemental analyses were performed on a THERMO SCIENTIFIC analyzer model Flash 2000. The Fourier-transform infrared (FTIR) spectra were measured on a BRUKER TENSOR 27 FT-IR and OPUS was used as the data collection program. UV-Vis absorption measurements were carried out at 298 K on a Cary100 UV-Vis spectrophotometer (Agilent Technologies, CA, USA) using a scan rate of 600 nm min^{-1}. The UV absorption spectra were acquired at 0.06 mM in water and 0.03 mM in diethyl ether (spectrum not shown) for 5-npic, and 0.02 mM in distilled water for metal complexes. The fluorescence spectra in solid state at room temperature were obtained on a Varian Cary-Eclipse spectrofluorometer equipped with a xenon lamp, Czerny–Turner monochromators, and a photomultiplier tube R-928. The powder X-ray diffraction (PXRD) patterns were collected on a BRUKER D8 DISCOVER diffractometer equipped with a PILATUS3R 100K-A detector and using CuKα radiation (λ = 1.5406 Å).

Single-crystal X-ray diffraction (SCRXD)

Single crystals of each compound were used for data collection. Diffraction intensities were recorded on a Bruker APEX-II CCD with a photon detector equipped with graphite monochromated MoKα radiation (λ = 0.71073 Å). The data reduction was performed with APEX2 software[53] and corrected for absorption using SADABS.[54] Crystal structures were solved by direct methods and refined by full-matrix least-squares with SHELXL-2019[55] using the OLEX2 crystallographic package.[56] The main refinement parameters of all compounds are summarized in Table S12.† CCDC numbers 2295415–2295420 contain the supplementary crystallographic data for this article.†

Theoretical calculations

Full geometry optimizations of the ground and excited states were performed with the Gaussian 16 program package (revision A.03)[57] using the hybrid exchange–correlation functional CAM-B3LYP.[58] The 6-31G** basis set was used for C, N, O, and H atoms and LANL2DZ[59] for Cd (complex **2**) and Zn (**6**) atoms. The vibrational frequencies were computed to check the absence of imaginary frequencies. The molecular geometries from SCRXD were taken as the starting point for geometry optimization in the ground state. The effect of the solvent was considered using the polarizable continuum model (PCM).[60] The vertical electronic transitions and geometry optimization of the excited electronic states were computed using time-dependent DFT calculations at the same level of theory. The fluorescence emission energy in solution from the first excited state was calculated at the same level of theory using $E_{em}(S_n) = E_{S_n}(G_{S_n}) - E_{S_0}(G_{S_n})$, where $E_{S_n}(G_{S_n})$ is the energy of the S_n state at its equilibrium geometry (G_{S_n}), in the state-specific solvation approach[61] and $E_{S_0}(G_{S_n})$ corresponds to the energy of the S_0 state at the S_n state geometry (G_{S_n}) and with the static solvation from the excited state.[62]

Two different approaches were used to simulate the crystallographic structure of **2** and **6** in order to interpret their photophysical properties. The D3 version of Grimme's dispersion correction (GD3zero damping) was included in the calculation.[63]

In the case of complex **2**, two finite fragments were selected considering one and four Cd metallic atoms, called **f1Cd** and **f4Cd**, respectively (Fig. S9†). The molecular geometries of these fragments were optimized in the ground state S_0 and first excited state S_1. The positions of some atoms were fixed to their corresponding crystallographic coordinates (Fig. S10†) to avoid large deformations of the fragment that lead to a departure from the original structure, while all other atoms of the fragment were allowed to relax during optimization. TD-DFT calculations were also performed for the **f1Cd** fragment (120 states) and **f4Cd** fragment (400 states).

The crystallographic structure of complex **6** was simulated using a two-layer ONIOM approach[64–66] building a model cluster containing 11 units from the SCXRD data. The central active molecule was treated with CAM-B3LYP-D3 (high level) and both S_0 and S_1 electronic state geometries were fully optimized (Fig. S11†). The central molecule was surrounded by 10 molecules (low level) treated semi-empirically using PM6[67] to alleviate the computational cost and with their molecular geometries frozen. The TD-DFT calculations were performed and 100 electronic transitions were computed. The vertical electronic transition for the emission was again calculated using $E_{em}(S_n) = E_{S_n}(G_{S_n}) - E_{S_0}(G_{S_n})$.

Cell culture and drug preparation

The anticancer properties were studied in three tumor cell lines: mouse melanoma cells B16-F10 (ATCC no. CRL-6475), human colorectal adenocarcinoma cell line HT29 (ECACC no. 9172201; ATCC no. HTB-38), and human hepatocarcinoma cell line HepG2 (ECACC no. 85011430). These cells were cultured in Dulbecco's Modified Eagle Medium (DMEM) supplemented with 2 mM glutamine, 10% heat-inactivated fetal bovine serum (FBS), 10 000 units per mL of penicillin, and 10 mg mL^{-1} of streptomycin. Then, they were incubated at 37 °C under 5% CO_2 atmosphere and 95% humidity.

Anti-inflammatory activities were studied in the monocyte/macrophage murine RAW 264.7 cell line (ATCC no. TIB-71). They were cultured in Roswell Park Memorial Institute 1640 (RPMI 1640) medium supplemented with 10% heat-inactivated fetal calf serum (FCS), 0.5 μg mL^{-1} gentamicin, being incubated at 37 °C under 5% CO_2 atmosphere and 95% humidity. All cells were grown to 80–90% of confluence in sterile cell culture flasks. Subconfluent monolayer cells were used in all experiments. The cells lines were provided by the cell bank of the University of Granada, Spain.

Compounds **1–6** and the 5-npic ligand were dissolved before use at 0.5 mg mL^{-1} in dimethyl sulfoxide (DMSO). A stock solution was frozen and stored at −20 °C. Prior to all the

experiments, this solution was diluted in the corresponding cell-culture medium.

Cell viability assay

The cell proliferation effect of each product in B16-F10, HT29, HepG2, and RAW 264.7 cells was quantified using the MTT assay (Sigma, MO, USA), which is based on the ability of living cells to cleave the tetrazolium ring, thus producing formazan, which absorbs at 570 nm. For this colorimetric assay, 5×10^3 B16-F10 cells, 6×10^3 HT29 cells, 15×10^3 HepG2 cells, and 6×10^3 RAW 264.7 cells were grown on a 96-well plate and incubated with increasing concentrations of ligand and compounds (0–100 μg mL^{-1}). After 72 h, 100 μL of MTT solution (0.5 mg mL^{-1}) in 50% PBS and 50% medium was added to each well. Finally, after 1.5 h of incubation, formazan was resuspended in 100 μL of DMSO, and each concentration was tested in triplicate. Relative cell viability, concerning untreated control cells, was measured by absorbance at 570 nm on an ELISA plate reader (Tecan Sunrise MR20-301, TECAN, Grödig, Austria). The concentrations at which these compounds inhibit the growth of 20, 50, and 80% of the cell population (IC_{20}, IC_{50}, and IC_{80}, respectively) were calculated.

Coordination compounds that showed high cytotoxicity for carcinogenic cell lines were further studied in apoptosis, cell cycle, and mitochondrial membrane potential tests.

Apoptosis analysis thought annexin V-FICT/PI flow cytometry

Apoptosis was analyzed with flow cytometry using a FACS flow cytometer (Coulter Corporation, Hialeah, FL, USA). Since best cytotoxic results were achieved with the B16-F10 cell line, for this assay, 5×10^4 B16-F10 cells were grown in 24-well plates with 1.5 mL of medium and incubated for 24 h. After this time, cells were treated with the selected complexes **2**, **4**, and the ligand 5-npic in triplicate for 72 h at IC_{50} and IC_{80}, calculated previously. The cells were collected and resuspended in binding buffer (10 mM HEPES/NaOH, pH 7.4, 140 mM NaCl, 2.5 mM $CaCl_2$). Annexin V-FITC conjugate (1 μg mL^{-1}) was then added and incubated for 15 min at room temperature in darkness. Just before analysis by flow cytometry, cells were stained with 5 μL of 1 mg mL^{-1} PI. In each experiment, approximately 10×10^3 cells were analyzed and the experiment was repeated twice.

Cell cycle analysis

The cell cycle was studied using PI staining by flow cytometry. This method was used to quantify the amount of DNA in the different phases of the cell cycle (G0/G1, S, and G2/M) using a FACS at 488 nm in an Epics XL flow cytometer. DNA content is directly proportional to the PI fluorescence. For this assay, 5×10^4 B16-F10 cells were plated in 24-well plates with 1.5 mL of medium and incubated for 24 h. Cells were treated with compounds **2**, **4**, and 5-npic in triplicate for 72 h, at their respective IC_{50} and IC_{80}. After treatment, the cells were washed twice with PBS, trypsinized and resuspended in TBS 1× (10 mM Tris and 150 mM NaCl). Then, Vindelov buffer (100 mM Tris, 100 mM NaCl, 10 mg mL^{-1} RNase, and 1 mg mL^{-1} PI, at pH 8) was added. Cells were stored on ice, and just before measurement, were stained with 10 mL of 1 mg mL^{-1} PI solution. In each experiment, approximately 10×10^3 cells were analyzed and the experiment was repeated twice.

Analysis of the mitochondrial-membrane potential (MMP)

Oxidative damage of the mitochondrial membrane caused by changes in its potential was studied by flow cytometry using dihydrorhodamine (DHR), which is oxidized to a fluorescent product, rhodamine (Rh123). Rh123 is a membrane-permeable, fluorescent cationic dye that is selectively taken up by the mitochondria and its fluorescence is proportional to the MMP. A negative Rh123 staining suggests an intrinsic apoptotic activation pathway, whereas a positive Rh123 staining means an extrinsic apoptotic pathway. Thus, the formation of Rh123 can be monitored by fluorescence spectroscopy using excitation and emission wavelengths of 500 and 536 nm, respectively. For this analysis, 5×10^4 B16-F10 cells were grown in 24-well plates with 1.5 mL of medium and incubated for 24 h. Cells were treated in triplicate with compounds **2**, **4** and 5-npic for 72 h at their respective IC_{50} and IC_{80}. After treatment, the culture medium was renewed with fresh medium by adding 0.5 μL of DHR, obtaining a final concentration of 5 μg mL^{-1}. Cells were then incubated for 1 h at 37 °C under a 5% CO_2 atmosphere and 95% humidity, and subsequently washed and resuspended in PBS with 5 μg mL^{-1} PI. The fluorescence intensity was measured using a FACScan flow cytometer.

Determination of NO production

RAW 264.7 cells are one of the most widely used models for studying inflammation *in vitro*. These cells produce the highest release of NO during the inflammatory response when stimulated by bacterial LPS. For the determination of NO production, the concentration of nitrites in the culture medium, used as an indicator, was evaluated according to the Griess reaction.[68] RAW 264.7 cells were plated at 6×10^4 cells per well in 24-well cell culture plates and supplemented with 10 μg mL^{-1} LPS. After 24 h, cells were incubated for 48 h with complexes **1–6** and 5-npic ligand at $\frac{3}{4}$ IC_{50}, $\frac{1}{2}$ IC_{50}, and $\frac{1}{4}$ IC_{50} values, previously calculated. The supernatants were collected to determine their nitrite concentration and/or stored at −80 °C for further use. The Griess reaction was performed taking 150 μL of supernatant test samples or sodium nitrite standard (0–120 μM) and mixed with 25 μL of Griess reagent A (0.1% *N*-(1-naphthyl)-ethylenediaminedihydrochloride) and 25 μL of Griess reagent B (1% sulfanilamide in 5% of phosphoric acid), in a 96-well plate. After 15 min of incubation at room temperature, the absorbance was measured at 540 nm in an ELISA plate reader (Tecan Sunrise MR20-301, TECAN, Austria). The absorbance was referred to the nitrite standard curve to determine the concentration of nitrite in the supernatant of each experimental sample. The percentage of NO production was determined, assigning 100% to the increase between the negative control (untreated cells) and positive control (cells only treated with 10 μg mL^{-1} of LPS).

Conclusions

In the present work, six different organometallic compounds based on Mn^{II}, Cd^{II}, Cu^{II}, Co^{II}, Ni^{II}, and Zn^{II} and the ligand 5-nitropicolinate were synthesized. They could be classified into three different groups according to their structures thanks to the diverse coordination modes of the 5-npic ligand. Single-crystal X-ray diffraction and FTIR analyses revealed that complexes **1** and **2**, with the formula $[M(5\text{-npic})_2]_n$, are monodimensional polymers along the *b* crystallographic axis; complex **3**, due to the Jahn–Teller distortion, forms a 2D polymer where the nitro group also coordinates to Cu^{II}; finally, complexes **4–6** are made up of mononuclear entities joined to one another by hydrogen bonds.

Complexes based on Cd^{II} and Zn^{II} have shown luminescence properties which would open the possibility of studying their localization in the cellular environment and monitoring their activity as drugs using bioimaging techniques. This advantage would be enhanced by the large Stokes shift observed for these compounds between the absorption and the emission spectra. The electronic transitions responsible for the photophysical properties were assigned by performing TD-DFT calculations. The analysis of the molecular orbitals involved in these transitions allowed us to conclude that the metallic centers do not participate in those transitions. This result, along with the similarity observed between the emission spectra of the ligand and those of compounds **2** and **6**, leads to the conclusion that the participation of the ligand–metal charge transfer processes would not be very significant or almost nil which would be an advantage in avoiding quenching of luminescence.

In addition, the anticancer properties of these compounds were analyzed against three cancer cell lines (B16-F10 murine melanoma cells, HT29 colon-cancer cells, and HepG2 hepatoma cells), highlighting the cytotoxic effect of compounds **2** and **4** in B16-F10, which improved the activity of 5-npic (2.5 and 1.5-fold better than that of the ligand for **2** and **4**, respectively). The apoptotic mechanism was demonstrated for both compounds with total apoptosis rates of 27.33 and 36.67% at IC_{50} and 58.40 and 93.95% at IC_{80} for **2** and **4**, respectively. Cell cycle analysis showed an arrest in the G0/G1 phase in response to the treatment for **4**, which could indicate a possible cytostatic or differentiation process. Finally, the MMP analysis suggested a potential activation of the intrinsic pathway during apoptosis of B16-F10 cancer cells caused by **2** and **4**. Considering these results, we hypothesize that the activation of apoptosis in response to compounds **2** and **4** might be mediated by the induction of cellular stress or genotoxicity, which would activate proteins such as p53 or p21. This mechanism would explain why compound **4** caused the cell cycle arrest in the G0/G1 phase. This initial process would be followed by changes in the expression of Bcl-2 family proteins, thereby leading to the disorganization of mitochondria and the loss of the MMP. Finally, the release of mitochondrial factors like cytochrome C or Apaf-1 would result in the formation of the apoptosome and the activation of caspase 9, culminating in the activation of caspase 3 and then, triggering the observed apoptotic phenomenon. Even though this is a very plausible mechanism of action for these compounds, additional studies are still warranted to draw definitive conclusions.

Regarding the anti-inflammatory potential, most of the compounds produced an inhibition of NO production under the assay conditions. Among them, compounds **2**, **3**, and **6** showed the highest inhibition values, being 1.25 to 5.6-fold more effective than the free ligand. Furthermore, complex **2** presented the lowest $IC_{50\ NO}$ concentration ($5.38 \pm 0.04\ \mu g\ mL^{-1}$).

Out of all the substances studied, the compound **2** ($[Cd(5\text{-npic})_2]_n$) had the strongest effect as anticancer and anti-inflammatory agent. In summary, the new synthesized complexes, highlighting compound **2** with both proapoptotic and anti-inflammatory properties, may offer a novel and effective approach to treat chronic inflammatory diseases, and tumorigenic and carcinogenic traits.

Author contributions

A. G.-G. performed the experiments and wrote the manuscript; M. M.-O., M. C.-M., and J. S. performed the biological experiments; J. M., M. M. Q.-M., and A. N. performed the theoretical calculations; I. J. V.-Y. carried out the single-crystal X-ray diffraction measurement and refinement; S. R., A. R.-D., and F. J. R.-Z. designed and supervised the study. All authors discussed the results, commented on the manuscript, and approved the final version.

Conflicts of interest

There are no conflicts to declare.

Acknowledgements

This work has been funded by Junta de Andalucía (FQM-394, P21_00386, BIO-157, PAIDI-FQM-337, ProyExcel_00386, and BFQM-650-ugr20) and TED2021-132440B-I00 funded by MCIN/AEI/10.13039/501100011033. The authors also thank Universidad de Jaén, FEDER_UJA_2020 (project 2021/00627/001) for supporting the research described in this article. M. M. Q.-M. and S. R thank Ministerio de Ciencia e Innovación for Ramón y Cajal contracts (the publication is part of the grants RYC2021-034288-I and RYC2021-032522-I, funded by MCIN/AEI/10.13039/501100011033 and by the European Union "Next Generation-EU"/"PRTR"). A. G.-G. also thanks the Ministerio de Universidades and Next-Generation funds for a Margarita Salas contract. Funding for open access charge: Universidad de Granada / CBUA.

References

1 K. D. Mjos and C. Orvig, *Chem. Rev.*, 2014, **114**, 4540–4563.
2 S. Dasari and P. B. Tchounwou, *Eur. J. Pharmacol.*, 2014, **740**, 364–378.
3 J. Liu, H. Lai, Z. Xiong, B. Chen and T. Chen, *Chem. Commun.*, 2019, **55**, 9904–9914.
4 A. Mantovani, P. Allavena, A. Sica and F. Balkwill, *Nature*, 2008, **454**, 436–444.
5 L. L. Munn, *Wiley Interdiscip. Rev.: Syst. Biol. Med.*, 2017, **9**, 1–13.
6 J. Perego, C. X. Bezuidenhout, I. Villa, F. Cova, R. Crapanzano, I. Frank, F. Pagano, N. Kratochwill, E. Auffray, S. Bracco, A. Vedda, C. Dujardin, P. E. Sozzani, F. Meinardi, A. Comotti and A. Monguzzi, *Nat. Commun.*, 2022, **13**, 1–10.
7 H. Ji, X. Wang, P. Wang, Y. Gong, Y. Wang, C. Liu, G. Ji, X. Wang and M. Wang, *J. Nanobiotechnol.*, 2022, **20**, 1–13.
8 K. H. Thompson and C. Orvig, *Dalton Trans.*, 2006, 761–764.
9 R. S. Grant, S. E. Coggan and G. A. Smythe, *Int. J. Tryptophan Res.*, 2009, **2**, 71–79.
10 C. L. Broadhurst and P. Domenico, *Diabetes Technol. Ther.*, 2006, **8**, 677–687.
11 R. Abarca, G. Gomez, C. Velasquez, M. A. Paez, M. Gulppi, A. Arrieta and M. I. Azocar, *Chin. J. Chem.*, 2012, **30**, 1631–1635.
12 M. Kalinowska, M. Borawska, R. Świsłocka, J. Piekut and W. Lewandowski, *J. Mol. Struct.*, 2007, **834–836**, 419–425.
13 Á. Raya-Barón, I. Oyarzabal, F. M. Arrabal-Campos, J. M. Seco, A. Rodríguez-Diéguez and I. Fernández, *Inorg. Chem.*, 2017, **56**, 8768–8775.
14 E. C. Constable, C. E. Housecroft, B. M. Kariuki and A. Mahmood, *Supramol. Chem.*, 2006, **18**, 299–303.
15 E. Matsumura, M. Ariga and T. Ohfuji, *Bull. Chem. Soc. Jpn.*, 1970, **43**, 3210–3214.
16 G. Świderski, M. Kalinowska, J. Malejko and W. Lewandowski, *Vib. Spectrosc.*, 2016, **87**, 81–87.
17 V. F. Zolin, L. N. Puntus, V. I. Tsaryuk, V. A. Kudryashova, J. Legendziewicz, P. Gawryszewska and R. Szostak, *J. Alloys Compd.*, 2004, **380**, 279–284.
18 H.-J. Xu and L. Xu, *Inorg. Chim. Acta*, 2013, **394**, 140–145.
19 L. Mao, S. J. Rettig, R. C. Thompson, J. Trotter and S. Xia, *Can. J. Chem.*, 1996, **74**, 2413–2423.
20 D. Dobrzyńska, L. B. Jerzykiewicz, J. Jezierska and M. Duczmal, *Cryst. Growth Des.*, 2005, **5**, 1945–1951.
21 Y. F. Huang, Z. W. Shi, Y. Liu, H. Xiao and X. H. Yin, *Russ. J. Coord. Chem.*, 2015, **41**, 325–333.
22 M. A. Halcrow, *Chem. Soc. Rev.*, 2013, **42**, 1784–1795.
23 M. A. Halcrow, *Dalton Trans.*, 2003, 4375–4384.
24 H. Ma, Y. Xu, Q. Meng, L. Zhang, R. Wang and D. Sun, *Z. Anorg. Allg. Chem.*, 2014, **640**, 1408–1412.
25 B. Zurowska and A. Kochel, *J. Mol. Struct.*, 2008, **877**, 100–104.
26 R. Pandey, D. Singh, N. Thakur and K. K. Raj, *ACS Omega*, 2021, **6**, 13240–13259.
27 W. Wei, Z. Liu, R. Wei, C. Liang, X.-Z. Feng and G.-C. Han, *J. Mol. Struct.*, 2021, **1228**, 1–11.
28 K. K. Gangu, S. Maddila, S. B. Mukkamala and S. B. Jonnalagadda, *Inorg. Chim. Acta*, 2018, **482**, 830–837.
29 A. T. Çolak, F. Çolak, O. Z. Yesilel, D. Akduman, F. Yilmaz and M. Tümer, *Inorg. Chim. Acta*, 2010, **363**, 2149–2162.
30 A. Suvitha, S. Periandy and M. Govindarajan, *Asian J. Phys.*, 2014, **23**, 1069–1078.
31 N. Kumar, Roopa, V. Bhalla and M. Kumar, *Coord. Chem. Rev.*, 2021, **427**, 1–14.
32 J. Li, R. Liu, J. Jiang, X. Liang, G. Huang, D. Yang, H. Chen, L. Pan and Z. Ma, *J. Inorg. Biochem.*, 2020, **210**, 1–13.
33 Z. Saedi, E. Hoveizi, M. Roushani, S. Massahi, M. Hadian and K. Salehi, *J. Mol. Struct.*, 2019, **1176**, 207–216.
34 S. Bibi, S. Mohamad, N. S. A. Manan, J. Ahmad, M. A. Kamboh, S. M. Khor, B. M. Yamin and S. N. A. Halim, *J. Mol. Struct.*, 2017, **1141**, 31–38.
35 L. E. Mihajlović-Lalić, J. Poljarević and S. Grgurić-Šipka, *Inorg. Chim. Acta*, 2021, **527**, 1–18.
36 A. Joshi, R. Gupta, K. Vaghasiya, R. K. Verma, D. Sharma and M. Singh, *ACS Appl. Bio Mater.*, 2020, **3**, 4025–4035.
37 D. Xu, Y. Xu, N. Cheng, X. Zhou, Y. Shi and Q. He, *J. Coord. Chem.*, 2010, **63**, 2360–2369.
38 I. Ivanović, S. Grgurić-Šipka, N. Gligorijević, S. Radulović, A. Roller, Ž. L. Tešić and B. K. Keppler, *J. Serb. Chem. Soc.*, 2011, **76**, 53–61.
39 N. Gligorijević, S. Aranđelović, L. Filipović, K. Jakovljević, R. Janković, S. Grgurić-Šipka, I. Ivanović, S. Radulović and Ž. L. Tešić, *J. Inorg. Biochem.*, 2012, **108**, 53–61.
40 S. Abdolmaleki, A. Aslani, A. Aliabadi, S. Khazayel, S. M. Amininasab, Z. Izadi, M. Ghadermazi, E. Motieiyan, D. Marabello and V. H. N. Rodrigues, *J. Coord. Chem.*, 2022, **75**, 147–161.
41 M. L. Matlou, F. P. Malan, S. Nkadimeng, L. McGaw, V. J. Tembu and A.-L. E. Manicum, *J. Biol. Inorg. Chem.*, 2023, **28**, 29–41.
42 A. F. A. Peacock, S. Parsons and P. J. Sadler, *J. Am. Chem. Soc.*, 2007, **129**, 3348–3357.
43 S. H. van Rijt, A. F. A. Peacock, R. D. L. Johnstone, S. Parsons and P. J. Sadler, *Inorg. Chem.*, 2009, **48**, 1753–1762.
44 H. Hao, X. Liu, X. Ge, Y. Zhao, X. Tian, T. Ren, Y. Wang, C. Zhao and Z. Liu, *J. Inorg. Biochem.*, 2019, **192**, 52–61.
45 M. J. Macazaga, J. Rodríguez, A. G. Quiroga, S. Peregina, A. Carnero, C. Navarro-Ranninger and R. M. Medina, *Eur. J. Inorg. Chem.*, 2008, **2008**, 4762–4769.
46 B. Fernández, I. Fernández, J. Cepeda, M. Medina-O'Donnell, E. E. Rufino-Palomares, Á. Raya-Barón, S. Gómez-Ruiz, A. Pérez-Jiménez, J. A. Lupiáñez, F. J. Reyes-Zurita and A. Rodríguez-Diéguez, *Cryst. Growth Des.*, 2018, **18**, 969–978.
47 K.-F. Chang, H.-C. Lai, S.-C. Lee, X.-F. Huang, Y.-C. Huang, T.-E. Chou, C.-Y. Hsiao and N.-M. Tsai, *J. Cell. Mol. Med.*, 2023, **27**, 1423–1435.
48 Z.-F. Zeng, Q.-P. Huang, J.-H. Cai, G.-J. Zheng, Q.-C. Huang, Z.-L. Liu, Z.-L. Chen and Y.-H. Wei, *Molecules*, 2021, **26**(13), 1–18.

49 L. K. Dillard, L. Lopez-Perez, R. X. Martinez, A. M. Fullerton, S. Chadha and C. M. McMahon, *Cancer Epidemiol.*, 2022, **79**, 1–10.
50 M. Balali-Mood, K. Naseri, Z. Tahergorabi, M. R. Khazdair and M. Sadeghi, *Front. Pharmacol.*, 2021, **12**, 1–19.
51 A. Sigel, H. Sigel and R. K. O. Sigel, *Cadmium: From toxicity to essentiality*, Springer, 2013, vol. 11.
52 S. Mahey, R. Kumar, M. Sharma, V. Kumar and R. Bhardwaj, *SN Appl. Sci.*, 2020, **2**, 1–12.
53 Bruker AXS Inc., 2004.
54 G. M. Sheldrick, *SADABS, Program for Empirical Absorption Correction of Area Detector Data*, University of Gottingen, Germany, 2010.
55 G. M. Sheldrick, *Acta Crystallogr., Sect. C: Struct. Chem.*, 2015, **71**, 3–8.
56 O. V. Dolomanov, L. J. Bourhis, R. J. Gildea, J. A. K. Howard and H. Puschmann, *J. Appl. Crystallogr.*, 2009, **42**, 339–341.
57 M. J. Frisch, G. W. Trucks, H. B. Schlegel, G. E. Scuseria, M. A. Robb, J. R. Cheeseman, G. Scalmani, V. Barone, G. A. Petersson, H. Nakatsuji and X. Li, *Gaussian* 16, Gaussian Inc., Wallingford, USA, 2016.
58 T. Yanai, D. P. Tew and N. C. Handy, *Chem. Phys. Lett.*, 2004, **393**, 51–57.
59 T. H. Dunning Jr. and P. J. Hay, *Modern Theoretical Chemistry*, Plenum Press, New York, 1977.
60 J. Tomasi, B. Mennucci and R. Cammi, *Chem. Rev.*, 2005, **105**, 2999–3093.
61 R. Improta, V. Barone, G. Scalmani and M. J. Frisch, *J. Chem. Phys.*, 2006, **125**, 1–9.
62 G. Scalmani, M. J. Frisch, B. Mennucci, J. Tomasi, R. Cammi and V. Barone, *J. Chem. Phys.*, 2006, **124**, 1–15.
63 S. Grimme, J. Antony, S. Ehrlich and H. Krieg, *J. Chem. Phys.*, 2010, **132**, 154104.
64 S. Dapprich, I. Komáromi, K. S. Byun, K. Morokuma and M. J. Frisch, *J. Mol. Struct.: THEOCHEM*, 1999, **461–462**, 1–21.
65 T. Vreven, K. Morokuma, Ö. Farkas, H. B. Schlegel and M. J. Frisch, *J. Comput. Chem.*, 2003, **24**, 760–769.
66 H. Lin and D. G. Truhlar, *Theor. Chem. Acc.*, 2007, **117**, 185–199.
67 J. J. P. Stewart, *J. Mol. Model.*, 2007, **13**, 1173–1213.
68 N. S. Bryan and M. B. Grisham, *Free Radicals Biol. Med.*, 2007, **43**, 645–657.
69 A. García-García, P. Cristobal-Cueto, T. Hidalgo, I. J. Vitórica-Yrezábal, A. Rodríguez-Diéguez, P. Horcajada and S. Rojas, Potential antiprostatic performance of novel lanthanide-complexes based on 5-nitropicolinic acid, *J. Biol. Inorg. Chem.*, 2024, DOI: **10.1007/s00775-024-02054-0**.